

# VibrantSR: Sub-Meter Canopy Height Models from Sentinel-2 Using Generative Flow Matching

Kiarie Ndegwa\*, Andreas Gros<sup>†</sup>, Tony Chang, David Diaz, Vincent A. Landau,  
 Nathan E. Rutenbeck, Luke J. Zachmann,  
 Guy Bayes<sup>†</sup>, Scott Conway

Vibrant Planet Public Benefit Corporation, Truckee, CA, USA

January 2026

## Abstract

We present VibrantSR (Vibrant Super-Resolution), a generative super-resolution framework for estimating 0.5 meter canopy height models (CHMs) from 10 meter Sentinel-2 imagery. Unlike approaches based on aerial imagery that are constrained by infrequent and irregular acquisition schedules, VibrantSR leverages globally available Sentinel-2 seasonal composites, enabling consistent monitoring at a seasonal-to-annual cadence. Evaluated across 22 EPA Level 3 eco-regions in the western United States using spatially disjoint validation splits, VibrantSR achieves a Mean Absolute Error of 4.39 meters for canopy heights  $\geq 2$  m, outperforming Meta (4.83 m), LANDFIRE (5.96 m), and ETH (7.05 m) satellite-based benchmarks. While aerial-based VibrantVS (2.71 m MAE) retains an accuracy advantage, VibrantSR enables operational forest monitoring and carbon accounting at continental scales without reliance on costly and temporally infrequent aerial acquisitions.

**Keywords:** canopy height model, canopy height super-resolution, flow matching, Sentinel-2, lidar, remote sensing, forest structure

## 1 Introduction

High-resolution canopy height models (CHMs) are a foundational geospatial layer for characterizing forest structure and its change over time. Sub-meter CHMs support operational tasks that depend on fine spatial detail—such as canopy gaps, edges, and within-stand heterogeneity—including fuels and wildfire planning [1, 2], biomass and carbon accounting [3], habitat assessment [4], and post-disturbance monitoring [5]. Many of these applications additionally require repeatable updates at a seasonal-to-annual cadence across large regions, rather than one-off, static maps [6].

Airborne lidar remains the most direct and accurate source of canopy height mapping. However, lidar acquisitions are spatially fragmented, costly to repeat frequently, and often temporally misaligned with rapidly evolving forest conditions driven by disturbance, management, and climate variability [7]. This creates a persistent trade-off between high-fidelity structural measurements where lidar exists and the need for broad, temporally consistent coverage that aligns with real-world monitoring and decision-making cycles [8]. Freely available satellite missions such as Sentinel-2 partially address the latter requirement by providing globally consistent multispectral imagery with regular revisit, but their native 10–60 m spatial resolution fundamentally under-resolves many canopy structural patterns that are critical at management scales [9].

---

\*Corresponding author: [kiarie@vibrantplanet.net](mailto:kiarie@vibrantplanet.net)

<sup>†</sup>Work carried out while at Vibrant Planet.

Recent machine learned canopy-height products illustrate this tension between accessible data and high spatial resolution requirements [10–12]. Global and continental-scale models trained using combinations of spaceborne and airborne lidar labels offer broad coverage, but typically operate at meter to tens-of-meters output resolution and rely on regression objectives that smooth out fine-scale canopy structure. While these approaches are effective for large-area summaries, the resulting predictions often suppress canopy gaps and attenuate height variability, distorting the structural distributions that downstream ecological and fire-behavior models depend on. As a result, while aerial imagery-based approaches set an upper bound on achievable accuracy for modeled canopy height, they do not fully satisfy the operational requirement for consistent, repeatable annual monitoring.

In our prior work, **VibrantVS**, we showed that high-resolution NAIP (National Agriculture Imagery Program) aerial imagery can support accurate 0.5 m canopy height estimation across diverse western United States eco-regions [13]. However, dependence on NAIP aerial imagery introduces practical constraints that include irregular and regionally heterogeneous acquisition schedules, infrequent revisit cadence (usually 2 years), and radiometric and geometric inconsistencies driven by flight-path variation and look-angle effects even within a single year. These factors limit suitability for frequent refresh cycles and global-scale deployment.

We introduce **VibrantSR** (*Vibrant Super-Resolution*), a generative framework for producing 0.5 m CHM from 10 m Sentinel-2 imagery. VibrantSR first derives compact representations of the Sentinel-2 inputs using separately pretrained, then frozen, feature extractors. A generative mapping then translates these Sentinel-2 representations into a high-resolution CHM representation learned from 0.5 m lidar-derived training targets, which is subsequently decoded into a 0.5 m CHM. By posing canopy-height inference as learning the distribution of plausible fine-scale structure conditioned on Sentinel-2, rather than predicting a single deterministic surface via pixel-wise regression, VibrantSR is encouraged to preserve realistic canopy variability that is often smoothed by existing satellite-based approaches. Full model and training details are provided in Section 4.

We evaluate VibrantSR on the western United States using spatially disjoint train and validation splits across EPA Level 3 eco-regions [14]. We focus on this region to ensure continuity with our prior VibrantVS benchmark, which was constructed exclusively over the western United States, enabling direct comparison under a consistent data, preprocessing, and evaluation protocol. We benchmark against VibrantVS as well as widely used satellite imagery-based CHM products [10–12].

Our objective is to demonstrate whether VibrantSR can offer reduced error compared to existing satellite-derived products for canopy heights  $\geq 2$  m while producing sharper, higher fidelity representations of canopy structure at sub-meter resolution and benchmark performance when compared to other well known modeled CHM products.

## 2 Related Work

### 2.1 Learning-Based Canopy Height Estimation

Deep learning methods for CHM estimation have evolved from convolutional neural networks to vision transformers [10, 12, 15]. Early approaches used regression losses to predict pixel-wise height values from aerial or satellite imagery. More recent work has explored self-supervised pretraining [10] and multi-task learning [13] to improve generalization across diverse forest types. Wagner et al. [15] demonstrated sub-meter tree height mapping using aerial images with a U-Net architecture informed by lidar. Our previous work, VibrantVS [13], introduced a multi-task vision transformer trained on NAIP aerial imagery that achieved state-of-the-art accuracy for CHM estimation in the western United States.

## 2.2 Operational CHM Products

Several operational CHM products are available for large-scale forest monitoring. These models adopt a regression-based canopy height estimation approach and typically predict conditional mean height surfaces from multispectral and ancillary inputs. Meta [10] uses Maxar Vivid2 imagery (0.5 m resolution) with a DINOv2-based architecture trained on NEON (National Ecological Observatory Network) lidar [16] and GEDI (Global Ecosystem Dynamics Investigation) data, providing 1 m resolution global coverage for 2020. LANDFIRE [11] employs a regression-tree based method using Landsat multi-spectral data along with topography and biophysical features at 30 m resolution with periodic updates. ETH [12] provides a deep learning ensemble trained on Sentinel-2 imagery with sparse GEDI lidar labels at 10 m resolution with global coverage.

## 2.3 Super-Resolution and Generative Models for Remote Sensing

Recent work has demonstrated that sub-meter predictions can be derived from Sentinel-2 imagery despite its 10 m native resolution. Sirko et al. [17] achieved 0.5 m resolution building and road segmentation from Sentinel-2 using teacher-student distillation, attaining 78.3% mIoU for building detection compared to 85.3% from high-resolution imagery. This work established that fine-scale spatial structure can be recovered from coarse satellite inputs when sufficient training signal is available.

More recently, generative models based on diffusion and flow-based formulations have been adopted for remote sensing super-resolution and image synthesis. These efforts have improved training stability and the ability to model complex, multi-modal output distributions compared to Generative Adversarial Networks (GANs). Latent diffusion models have been applied to Sentinel-2 super-resolution and harmonization tasks, where operating in a compressed latent space substantially reduces computational cost while preserving spatial and spectral fidelity [18–20].

In parallel, diffusion and score-based models have been explored for the generative downscaling of continuous geophysical fields in climate and weather applications, where the objective is not only visual realism but the preservation of physically meaningful spatial variability and distributional properties [21, 22]. Diffusion models and flow matching approaches offer advantages over GANs in training stability and sample diversity [23, 24]. Recent work has shown that rectified flow models scale predictably to high-resolution image synthesis when paired with a transformer backbone [25], demonstrating their suitability for high-capacity generative tasks. However, existing applications of flow matching and diffusion in Earth observation have largely focused on image-domain outputs or same-modality super-resolution, rather than the generation of biophysical structure fields.

To our knowledge there has not been any work adopting a latent generative formulation to model a full conditional distribution of fine-scale canopy structure based on a multispectral satellite image, thus motivating our adoption of this framework for CHM super-resolution.

## 3 Study Area and Data

This study builds directly on the study area definition and spatial data partitioning introduced in our prior work, VibrantVS [13]. We therefore summarize only the key aspects relevant to VibrantSR and refer readers to Chang et al. [13] for full details.

### 3.1 Sentinel-2 Imagery

VibrantSR uses 12-band Sentinel-2 Level-2A surface reflectance imagery [9], specifically the Sentinel-2C1-L2A collection distributed by Element84 [26]. We aggregated observations via a temporal

median over the 2024 temperate summer months (June–August) after masking individual acquisitions to remove clouds using the Scene Classification Layer (SCL) that is served alongside the data.

This temporal median aggregation reduces transient artifacts (e.g., residual cloud contamination) and captures vegetation structure during the peak temperate growing season. Inputs from all Sentinel-2 bands were processed and resampled to 10 m resolution using nearest neighbor interpolation; each training sample consisted of a  $48 \times 48$  Sentinel-2 image ( $480 \text{ m} \times 480 \text{ m}$ ) at 10 m resolution paired with a corresponding  $960 \times 960$  CHM tile at 0.5 m resolution. Sentinel-2 inputs were then standardized to zero mean and unit variance based on dataset statistics.

### 3.2 Ground-Truth CHMs

Ground-truth CHMs were derived from United States USGS 3D Elevation Program (3DEP) airborne lidar acquisitions [27]. CHMs were computed as the difference between the digital surface model (DSM) and digital terrain model (DTM), representing height above ground [28]. All metrics are provided for canopy heights at or above 2 m, following common practice in lidar applications in forest ecosystems to differentiate tree canopy from shrub and other non-tree vegetative cover. The preprocessing of these ground-truth CHMs were minimal: we applied min-max normalization to rescale height values to the target range of the autoencoder. We excluded tiles containing negative height values or open water to restrict training and evaluation to terrestrial vegetation. Heights exceeding biologically plausible limits were clipped to a maximum of 120 m to ensure stable training.

### 3.3 Evaluation Protocol

We employed a spatially disjoint “checkerboard” split to ensure the model was evaluated on geographically distinct areas (Fig. 1). This prevents spatial autocorrelation from inflating performance metrics. The final dataset was comprised of 168,834 training tiles and 66,154 validation tiles over 4,135 square kilometers, spanning 22 EPA Level 3 eco-regions [14] in the western United States and ensuring evaluation across diverse forest types, climate zones, and topographic conditions (Fig. 2).

## 4 Methods

### 4.1 Modeling Description

VibrantSR employs a generative flow matching architecture operating in compressed latent space (Fig. 3). The pipeline consists of three components: (1) a frozen Sentinel-2 autoencoder that compresses 12-channel inputs into a compact latent representation; (2) a trainable flow matching network that transforms Sentinel-2 latents into CHM latents; and (3) a frozen CHM autoencoder decoder that reconstructs 0.5-meter predictions from the generated latents.

The flow matching network is a U-shaped Vision Transformer (U-ViT) configured for velocity prediction. The architecture uses a linear flow path and was trained to minimize the velocity matching loss between the source (Sentinel-2 latent) and target (CHM latent) distributions. The model operates on  $32 \times 32$  latent grids using patch size 1, with 16 transformer layers and 16 attention heads. This high-capacity configuration allows the model to capture complex structural dependencies. Unlike regression-based methods that minimize pixel-wise error, this generative formulation enables the model to produce realistic canopy structures that preserve natural height distributions. Recent work [25] has demonstrated that rectified flow scales predictably for high-resolution image synthesis, motivating our adoption of this framework.

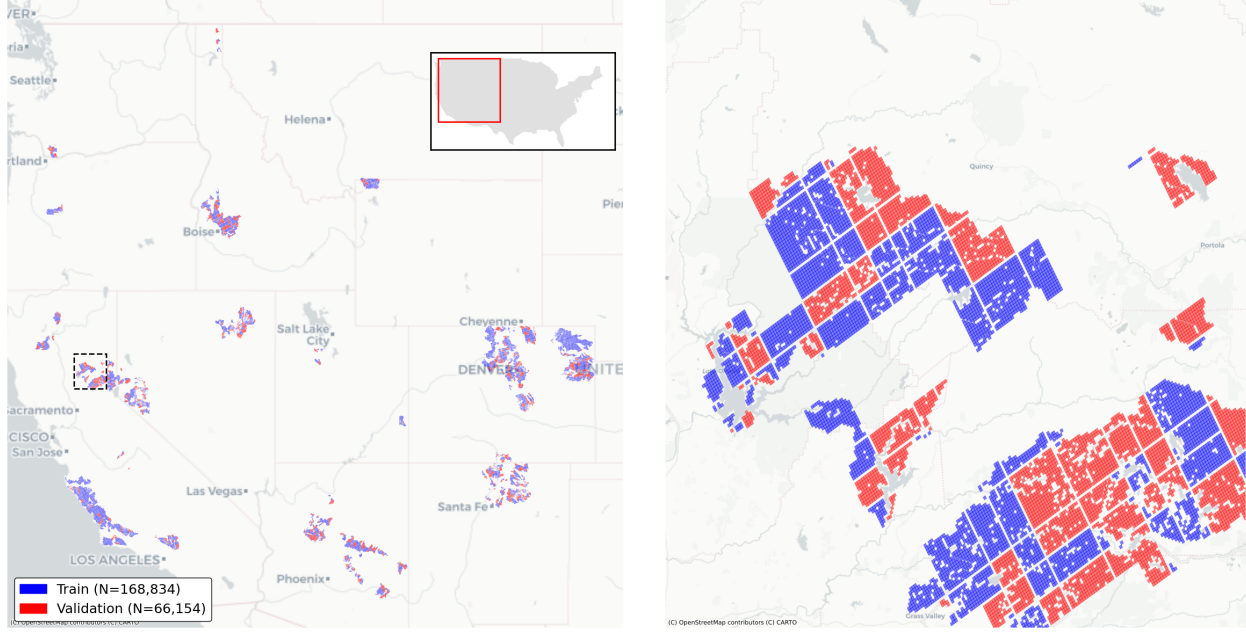


Figure 1: Spatial partitioning of training and validation tiles across the western United States. The left panel shows the distribution of tiles assigned to the training (blue) and validation (red) folds. The right panel provides a regional zoom illustrating strict spatial separation between folds.

US EPA L3 ecoregion	VibrantSR		Mean Error		Mean Absolute Error		Block R <sup>2</sup>		Root Mean Squared Error		Edge Error Metric		
	Meta	VibrantVS	VibrantSR	Meta	VibrantVS	VibrantSR	Meta	VibrantVS	VibrantSR	Meta	VibrantVS	VibrantSR	
Arizona/New Mexico Mountains	-2.4	-4.2	-1.5	0.6	-1.5	3.4	5.5	3.2	5.1	6.2	-0.63	-0.40	-0.50
Arizona/New Mexico Plateau	-2.2	-2.9	-0.3	-0.4	-3.3	2.6	3.0	1.3	2.4	3.7	-0.60	-3.50	-0.30
Cascades	-2.3	5.6	-5.0	1.6	12.0	8.9	8.5	7.0	9.6	13.5	-0.66	-0.70	-0.80
Central Basin and Range	-2.2	-2.9	-0.6	-2.0	-2.7	2.6	3.0	1.8	3.1	3.5	-0.76	-3.20	-0.40
Central California Foothills and Coastal Mountains	-1.8	-3.0	-0.9	5.0	8.6	3.6	3.9	1.7	9.6	9.0	-0.51	-0.60	-0.80
Chihuahuan Deserts	-1.7	-2.7	-2.0	-2.7	-2.5	1.9	2.7	2.8	2.8	2.8	-0.68	-1.90	-1.40
Colorado Plateaus	-1.9	-2.6	-0.3	-1.0	-3.3	2.1	2.8	1.3	2.5	3.3	-0.75	-3.00	-0.50
High Plains	-2.7	5.4	-1.5	-5.3	-0.8	4.1	5.5	2.5	6.2	4.4	-0.47	-2.50	-0.10
Idaho Batholith	-2.9	-6.0	-1.6	0.7	12.3	7.2	7.9	4.4	7.9	12.9	-0.49	-0.20	-0.90
Klamath Mountains/California High North Coast Range	-1.5	5.0	-2.1	3.3	11.8	7.8	7.0	4.2	9.1	12.5	-0.66	-0.60	-0.90
Madrean Archipelago	-2.1	-2.9	-1.6	-2.4	-2.8	2.4	3.0	2.5	3.0	3.3	-0.77	-4.50	-1.80
Middle Rockies	-2.9	6.0	-1.9	0.9	7.5	5.6	6.7	3.7	6.5	8.2	-0.60	-0.40	-0.80
Mojave Basin and Range	-2.6	-3.0	-0.9	-2.9	-2.9	3.2	3.1	1.7	3.1	3.0	-0.61	-2.90	-0.40
Northern Rockies	-1.2	4.7	-1.5	4.5	9.9	7.9	7.0	5.0	7.5	10.4	-0.85	-0.90	-0.90
Sierra Nevada	-3.0	-6.9	-1.3	4.7	10.8	9.1	8.9	5.1	10.0	11.7	-0.62	-0.50	-0.90
Snake River Plain	-2.0	-3.1	-0.3	-0.4	7.6	2.7	3.5	1.7	4.8	7.9	-0.43	-1.10	-0.70
Sonoran Basin and Range	-2.2	-2.7	-0.8	-2.4	-2.6	2.2	2.8	1.5	2.7	2.7	-0.71	-1.60	-0.10
Southern California Mountains	-1.8	-2.7	-0.6	4.4	8.2	3.2	3.4	1.3	8.8	8.4	-0.66	-2.10	-0.30
Southern Rockies	-2.6	4.3	-0.9	3.3	7.6	5.0	5.1	3.0	5.6	8.1	-0.65	-0.00	-0.80
Southwestern Tablelands	-2.1	-3.2	-0.1	-3.1	-2.1	3.2	3.7	2.1	5.1	3.6	-0.59	-1.20	-0.20
Willamette Valley	-3.1	7.4	-5.3	-1.8	13.2	8.4	9.0	6.6	10.2	14.0	-0.46	-0.50	-0.70
Wyoming Basin	-4.1	-7.6	-0.6	1.7	4.8	5.9	7.7	3.0	4.0	6.3	-0.60	-1.30	-0.90

Figure 2: Error metrics across EPA Level 3 ecoregions.

VibrantSR was trained in a staged manner. The Sentinel-2 encoder and CHM autoencoder were each pretrained independently prior to training the flow matching model, and their parameters were frozen in all subsequent experiments.

The Sentinel-2 autoencoder was pretrained on Sentinel-2 imagery drawn from the same geographic regions as the downstream task. The overall architecture supports Sentinel-2 inputs at arbitrary temporal resolution or aggregations, including seasonal composites or single-date acquisitions, once trained for the corresponding input distribution. Its purpose is to compress multi-spectral inputs into a latent representation that preserves spatial and spectral context relevant for canopy height inference, while reducing the dimensionality of the generative modeling problem.

The CHM autoencoder was pretrained separately on lidar-derived canopy height tiles from the same study area. The decoder learns to reconstruct high-resolution canopy height fields from latent representations that capture fine-scale vertical structure.

By pretraining both components independently and freezing them thereafter, the flow matching network is trained to learn a transport map between two fixed and compatible latent manifolds. This staged training strategy isolates the contribution of the flow matching model and avoids entangling representation learning with generative transport, enabling more stable training and clearer attribution of performance gains.

At inference time, the conditional Sentinel-2 latent is concatenated with an input-conditioned noise vector, ensuring that identical inputs yield identical outputs while retaining the expressivity of the generative model.  $\frac{dz}{dt} = v_\theta(z, t)$  is then integrated from  $z(0) = x$  to  $t = 1$  using the `dopri5` ODE solver with 100 integration steps [29, 30]. No additional stochasticity is introduced during integration, and outputs are fully reproducible for a given input.

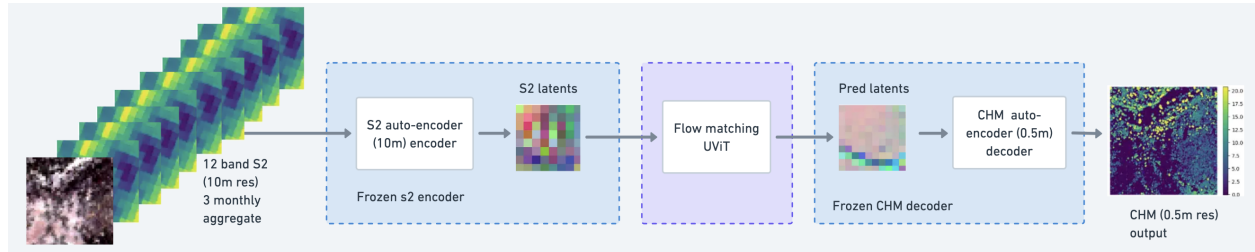


Figure 3: VibrantSR architecture showing the flow from Sentinel-2 inputs through frozen autoencoders and the trainable flow matching network to CHM outputs.

## 4.2 Experimental Setup

We trained the flow matching model using AdamW with a batch size of 16. Random horizontal and vertical flips, along with 90-degree rotations, were applied on-the-fly to paired Sentinel-2 and CHM tiles before encoding. The Sentinel-2 and CHM autoencoders were pretrained separately and frozen during flow matching training. Training was performed on a single node equipped with 8×NVIDIA A100 GPUs. Total training compute was approximately 5,400 A100-hours across all model components.

We compare **VibrantSR** against four baseline CHM products with differing input modalities, coverage, and spatial resolution (Table 1).

Table 1: Baseline model comparison.

Model	Resolution	Input Data	Coverage
VibrantVS [13]	0.5 m	NAIP aerial	Western United States
Meta [10]	1 m	Maxar Vivid2	Global
LANDFIRE [11]	30 m	Landsat	United States
ETH [12]	10 m	Sentinel-2	Global

We evaluated performance using four metrics: Mean Absolute Error (MAE), Mean Error (ME) indicating systematic bias, Block-R<sup>2</sup> measuring explained variance at an aggregated spatial scale, and Edge Error (EE) measuring structural fidelity via Sobel edge comparison [10]. Formal definitions are provided in the Appendix. Block-R<sup>2</sup> was computed by aggregating predictions and ground truth over non-overlapping 30 × 30 meter blocks in the CHM domain, corresponding to approximately 15 m × 15 m ground area at 0.5 m resolution.

## 5 Results

### 5.1 Quantitative Comparison

VibrantSR achieves an average Mean Absolute Error of 4.39 meters for canopy heights  $\geq 2$ m across the test fold, outperforming all satellite imagery-based models (Meta, LANDFIRE, and ETH; Table 2). VibrantSR reduces MAE by 9% relative to Meta (4.39 m vs 4.83 m), 26% relative to LANDFIRE (4.39 m vs 5.96 m), and 38% relative to ETH (4.39 m vs 7.05 m). VibrantSR also achieves substantially lower edge error than these three models, indicating superior structural fidelity.

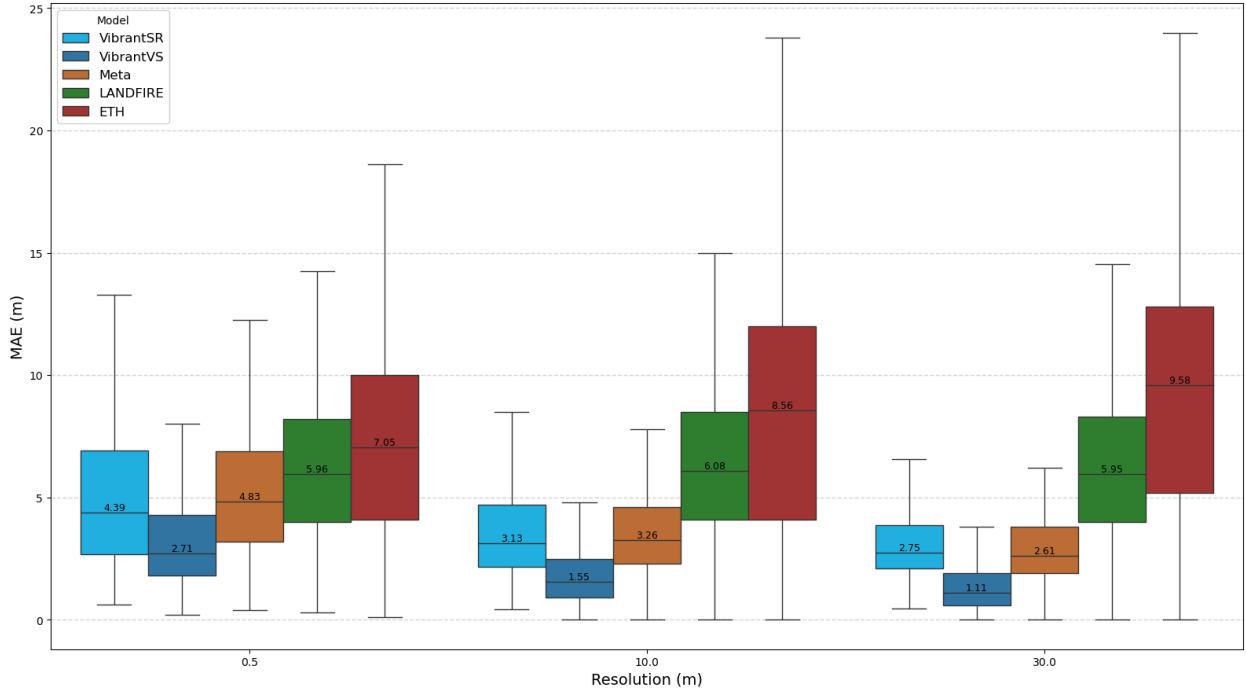


Figure 4: Mean absolute error (MAE) as a function of output resolution for VibrantSR and baseline CHM products. Box-whisker plots summarize tile-level error at 0.5 m, 10 m, and 30 m. VibrantSSR maintains stable accuracy across resolutions.

Table 2: Performance comparison across models at 0.5 m resolution. All metrics computed for heights  $\geq 2$  m.

Model	MAE	Mean Error	Block-R <sup>2</sup>	Edge Error
<b>VibrantSR</b>	<b>4.39</b>	<b>-2.35</b>	<b>-0.62</b>	<b>0.16</b>
VibrantVS	2.71	-1.11	0.69	0.08
Meta	4.83	-4.03	-0.60	0.30
LANDFIRE	5.96	0.92	-1.45	0.63
ETH	7.05	5.65	-1.85	0.64

Performance improvement relative to other satellite imagery-based models is mostly consistent across diverse EPA Level 3 eco-regions (Fig. 5). In addition to aggregate error metrics, we show residuals stratified by canopy height to assess how errors vary across the height distribution (Fig. 5).

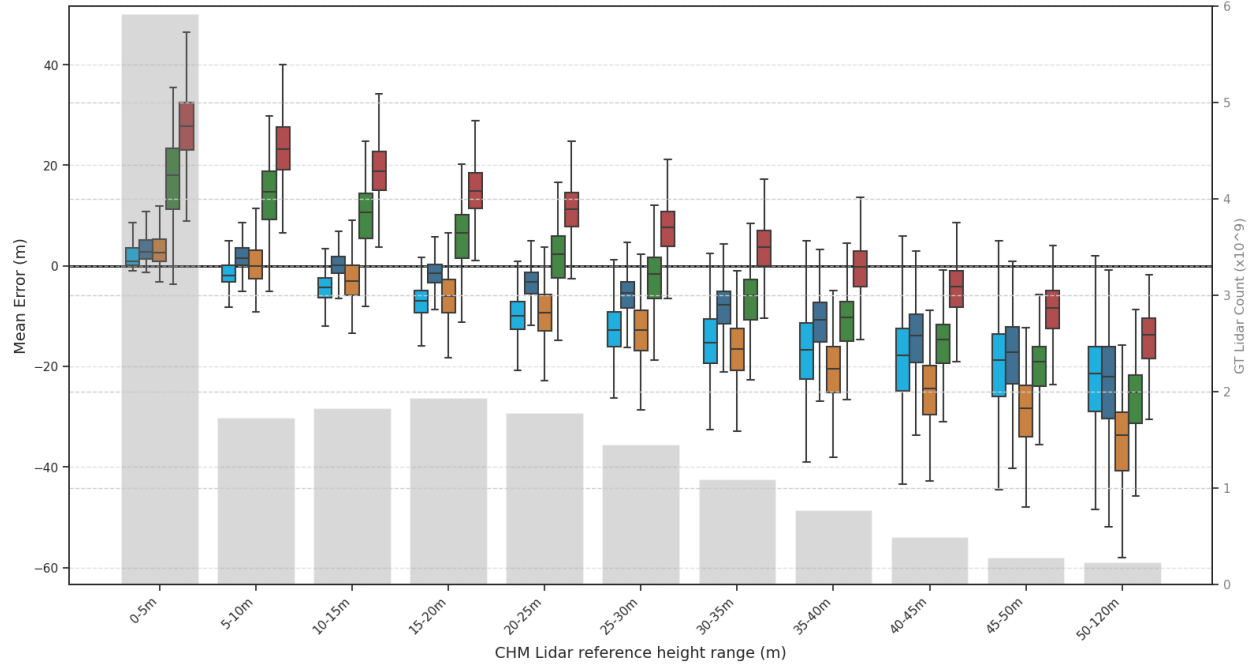
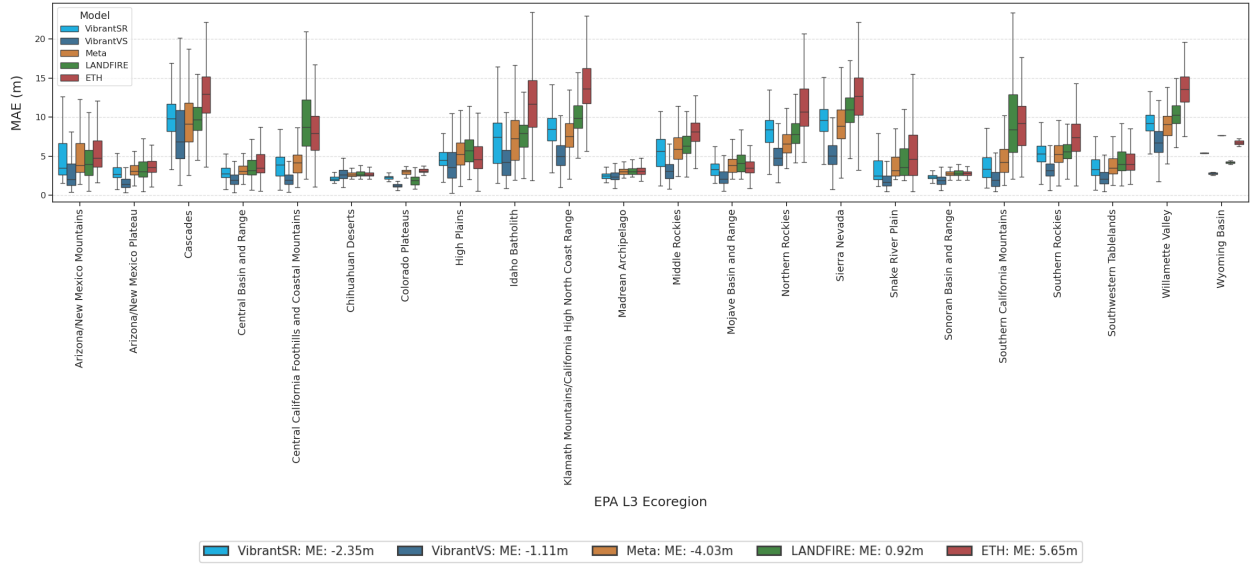


Figure 5: **(Top)** Mean absolute error (MAE) by EPA Level-3 ecoregion for VibrantSR and competing CHM products. Each box-whisker summarizes the distribution of tile-level MAE within an ecoregion at 0.5 m resolution. VibrantSR is consistently among the lowest-error methods in structurally complex, high-biomass regions (e.g., Rockies, Sierra Nevada, Cascades), while performance converges in flatter and sparsely vegetated regions. **(Bottom)** Height-binned distribution of per-pixel canopy-height error ( $\hat{h} - h$ ) at 0.5 m resolution. Boxes show the interquartile range, horizontal lines indicate the median, and whiskers denote the 5th–95th percentiles; grey bars give the relative lidar sample count. VibrantSR shows a smooth shift toward increasing underestimation with height, whereas LANDFIRE and ETH exhibit larger and less stable biases, particularly at low and very high canopy heights.

## 5.2 Qualitative Results

Figure 6 shows side-by-side comparison of input Sentinel-2 imagery (10 m), ground-truth lidar CHM (0.5 m), and VibrantSR prediction (0.5 m) along with predictions from other models. VibrantSR uses coarse spectral inputs to generate plausible sub-meter canopy structure—including gaps and edges—that is typically smoothed by regression-based approaches. VibrantSR also closely matches the ground-truth distribution of canopy heights (Figs. 7), indicating the generative approach captures realistic structural variability rather than simply smoothing predictions toward the mean.

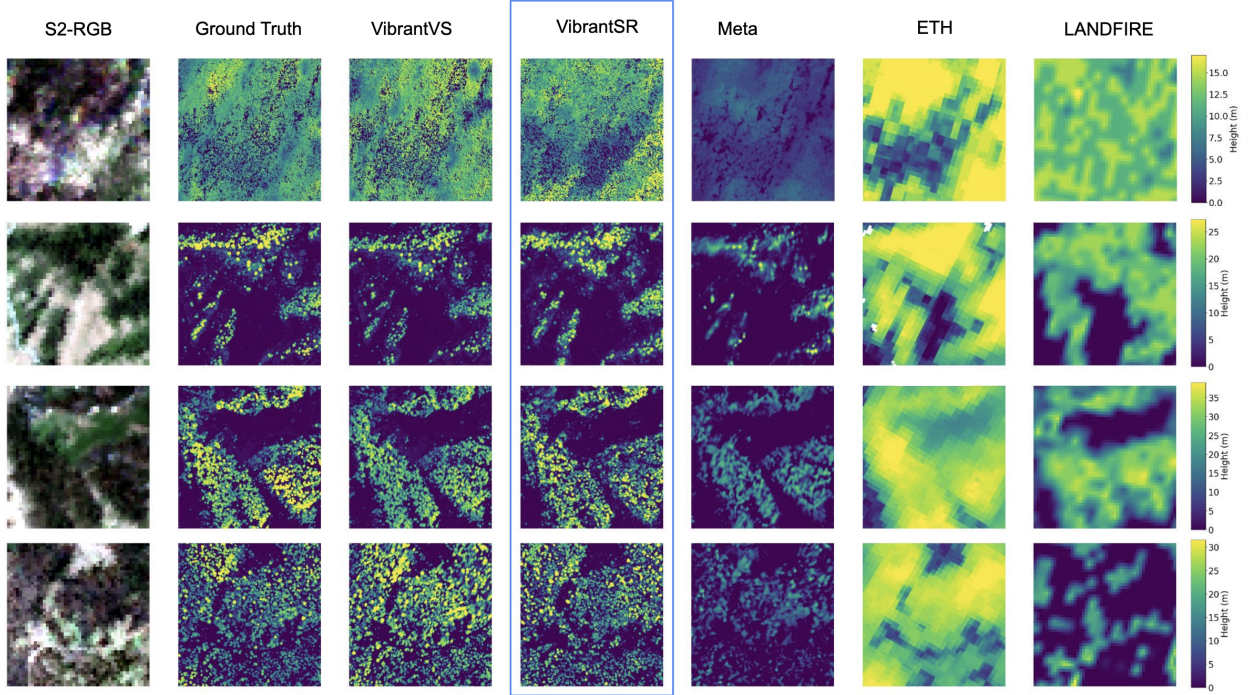


Figure 6: Qualitative comparison of canopy-height predictions across multiple regions (one region per row). Within each row, all panels correspond to the same region; Sentinel-2 RGB is included among the **VibrantSR** input bands, whereas the other methods use their respective native input modalities.

## 6 Discussion

VibrantSR decouples high-resolution CHM estimation from aerial imagery, enabling broad deployment with seasonal-to-annual update frequency. The generative approach helps synthesize fine-grained canopy gaps and height distributions that are often smoothed by regression-based methods, and the model generalizes well across diverse forest types and climate zones. This represents a significant advance over existing satellite-based products: while ETH [12] and LANDFIRE [11] provide broader coverage, their coarser resolution (10–30 m) limits utility for fine-scale forest management decisions. VibrantSR bridges this gap by achieving sub-meter output resolution from freely available global imagery. However, VibrantVS (2.71 m MAE) retains a significant accuracy advantage over VibrantSR (4.39 m MAE), reflecting the fundamental information loss in 10 m vs 0.5 m input resolution. This gap is unlikely to be closed through architectural improvements alone; the spectral information in Sentinel-2 imagery quarterly aggregates cannot uniquely determine sub-meter canopy structure. However, for many landscape-based uses, the current residual remains

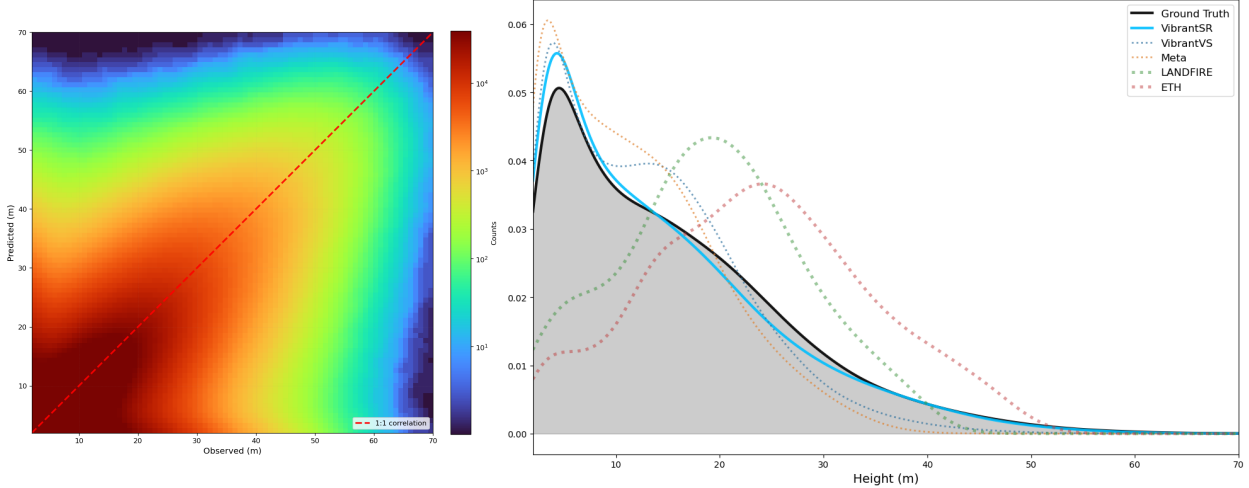


Figure 7: Distributional agreement between lidar reference canopy heights and model predictions for pixels with reference CHM  $\geq 2$  m. **(Left)** Joint distribution of ground truth versus **VibrantSR** predictions. **(Right)** Kernel density estimates of canopy-height distributions for ground truth and predictions from **VibrantSR**, **VibrantVS**, Meta, LANDFIRE, and ETH.

acceptable.

The choice of generative flow matching over regression-based approaches merits discussion. Traditional CHM models trained with MSE loss tend to produce smoothed predictions that regress toward the mean losing the high-frequency structural detail critical for applications such as individual tree detection and canopy gap mapping. Our distribution matching results (Figs. 7) demonstrate that VibrantSR preserves the natural variability of canopy heights, a property that emerges from the generative formulation rather than explicit structural losses. This suggests that flow matching may be broadly applicable to remote sensing tasks where preserving distributional properties is important. The negative Block- $R^2$  (Table 2) indicates that, under a pixel-wise variance-explained metric, predictions do not match ground truth at the chosen scale of spatial aggregation. We attribute this in part to a double-penalty effect: when high-frequency structure is slightly shifted relative to the label, pixel-wise metrics penalize it both as a false positive and a false negative, which can drive  $R^2$  negative even when the predicted height distribution and texture are visually plausible. For most of the intended use cases for VibrantSR, distributional agreement (Figs. 7) and residual analysis are therefore complementary and often more relevant indicators than strict pixel-level correspondence.

Several limitations should be noted when interpreting and applying VibrantSR outputs. First, the evaluation is currently limited to the western United States. While the eco-regions cover a diverse range of forest types, performance in tropical or boreal forests with different structural characteristics remains to be validated. Second, the temporal mismatch between available lidar training data and the 2024 Sentinel-2 imagery introduces noise in both training and evaluation. Although we prioritize recent lidar collections, the rapidly changing nature of forest structure due to disturbance means that some training labels may not accurately reflect the current state of the canopy seen by the satellite. Third, the reliance on optical Sentinel-2 imagery means that the model cannot “see” through clouds or dense smoke. While our seasonal aggregation strategy mitigates this, persistent cloud cover in some regions may result in data gaps or lower-quality predictions. Qualitative inspection also reveals failure modes common to optical satellite-based monitoring (Fig. 8): model hallucination is observed primarily in areas with very tall, dense canopy where the Sentinel-2 signal saturates, and sharp boundaries at forest edges can appear blurred due to

mixed-pixel effects.

To reduce these effects in future work, we will (i) avoid median-composited inputs in favor of per-date Sentinel-2 observations to preserve fine spatial structure, (ii) leverage multiple temporally independent observations of the same location and regularize predictions to be consistent across acquisitions, and (iii) include additional supervision focused on regions and tiles where hallucinations are repeatedly observed.

A related constraint is that we intentionally avoid conditioning on GEDI and on other ancillary sensors in the current model. While GEDI provides valuable vertical-structure information, its sampling is sparse and uneven, and incorporating it would require a more complex multi-modal framework with careful spatiotemporal co-registration, explicit handling of missing data, and robustness to differing coverage patterns across regions and years. In practice, this can introduce additional sources of bias and complexity, and reduce deployability by coupling predictions to the availability and stability of an extra modality.

Finally, the 0.5 m output resolution, while structurally plausible, is a generative super-resolution from 10 m inputs. The fine-scale details are synthesized based on learned distributions and should be interpreted as statistically representative realizations rather than exact physical measurements. Outputs should not be treated as a substitute for field surveys or lidar in regulatory, legal, or safety-critical contexts, nor used for fine-scale operational decisions such as tree-level hazard assessment.

VibrantSR occupies a distinct niche in the landscape of canopy height products, and practitioners should select among available options based on their specific requirements. For project-level planning requiring the highest accuracy—such as individual fuel break design or precise thinning prescriptions—VibrantVS or direct lidar acquisition remain preferable. However, for regional screening, prioritization, and monitoring applications where broad coverage and temporal consistency matter more than sub-meter precision, VibrantSR offers a practical solution. The seasonal-to-annual update capability enables before-and-after disturbance comparisons and multi-year trend analysis that are not possible with static products like Meta or LANDFIRE. The approach is well-suited as a screening layer to identify priority areas for targeted lidar acquisition or field validation, rather than as a standalone decision tool. By enabling sub-meter canopy height inference from freely available Sentinel-2 imagery, VibrantSR lowers barriers to accessing structurally detailed forest information, with particular relevance for regions with limited resources for airborne data acquisition.

## 7 Conclusion

We introduced **VibrantSR**, a generative flow-matching approach that produces 0.5 m canopy height models (CHMs) from 10 m Sentinel-2 imagery. Across 22 EPA Level 3 ecoregions in the western United States, VibrantSR attains a mean absolute error of 4.39 m for reference canopy heights  $\geq 2$  m, corresponding to a 9–38% reduction in error relative to widely used satellite-based CHM baselines (Meta, LANDFIRE, ETH). Beyond aggregate accuracy, the generative formulation better preserves canopy-height distributions and fine-scale structural detail, yielding lower edge error and closer agreement with lidar-derived reference statistics than regression-based alternatives.

VibrantSR helps address a key limitation in large-area forest monitoring: the scarcity of high-resolution structural estimates with consistent, repeatable temporal coverage. By avoiding dependence on aerial imagery acquisition, the method enables seasonal-to-annual CHM updates from globally available satellite observations. While aerial-imagery approaches such as VibrantVS remain preferable for site-specific analyses where airborne inputs are available, VibrantSR offers a practical capability for regional screening, change detection, and carbon accounting at continental scales.

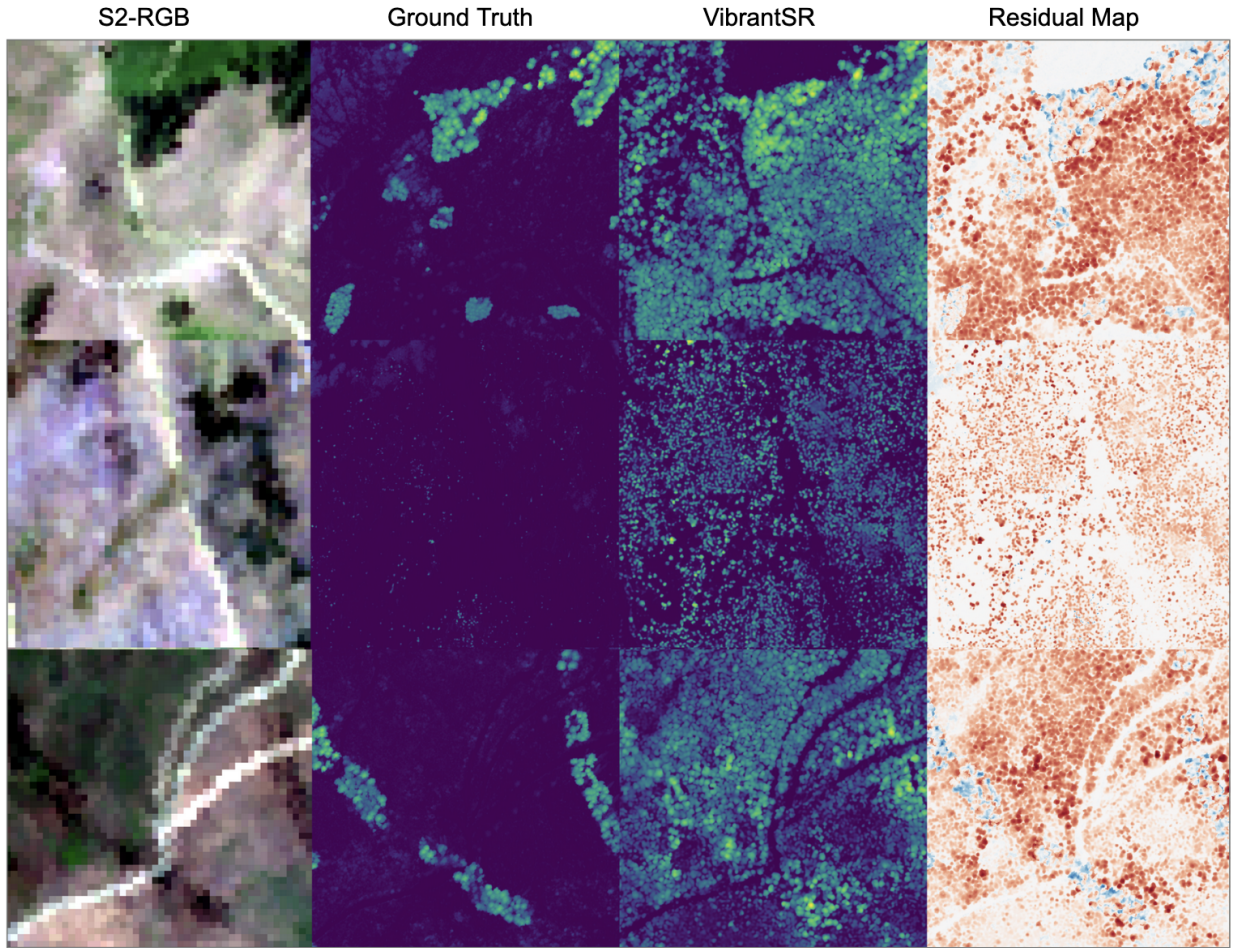


Figure 8: Failure modes in regions containing tall trees. From left to right: color corrected RGB Sentinel-2 summer aggregate inputs, the ground-truth lidar-derived CHM, super-resolved synthetic CHM, and an error heatmap (reds=overestimation, blues=underestimation) displaying hallucinated height predictions.

Future work will broaden evaluation to additional forest biomes, train with multi-seasonal aggregates to support year-round inference, and incorporate auxiliary modalities (e.g., SAR) to further reduce error. We will also mitigate the dominant optical failure modes in tall, dense canopies and along sharp forest boundaries by (i) replacing median-composited inputs with per-date Sentinel-2 observations to better preserve fine spatial structure, (ii) leveraging multiple temporally independent acquisitions with consistency regularization across observations, and (iii) adding targeted supervision for regions and tiles where hallucinations recur.

## 8 Author Contributions

Conceptualization, K.N., A.G. and T.C.; methodology, K.N.; data curation, V.A.L. and L.J.Z.; writing—review and editing, K.N., A.G., D.D., N.E.R., T.C., V.A.L., and L.J.Z.; project administration, T.C., N.E.R., G.B and S.C. Author order for D.D., V.A.L, N.E.R. and L.J.Z. is alphabetical by last name.

## Data Availability

Ground-truth canopy height models are derived from the dataset introduced in VibrantVS [13], which is publicly available. Sentinel-2 Level-2A imagery is freely accessible via the Copernicus Open Access Hub and Google Earth Engine. Model architecture, and inference code will be made available upon publication.

## A Metric Definitions

**Mean Absolute Error (MAE):**

$$\text{MAE} = \frac{1}{n} \sum_{i=1}^n |y_i - \hat{y}_i|$$

**Mean Error (ME):**

$$\text{ME} = \frac{1}{n} \sum_{i=1}^n (\hat{y}_i - y_i)$$

**Block-R<sup>2</sup>:**

$$R^2_{\text{block}} = 1 - \frac{\sum_{b=1}^B \sum_{i \in b} (y_i - \hat{y}_i)^2}{\sum_{b=1}^B \sum_{i \in b} (y_i - \bar{y}_b)^2}$$

**Edge Error (EE):**

$$\text{EE} = \frac{1}{n} \sum_{i=1}^n |E(\hat{y}_i) - E(y_i)|$$

where  $E(\cdot)$  represents the Sobel edge detection operation.

## References

- [1] Malcolm P. North, Robert A. York, Brandon M. Collins, Matthew D. Hurteau, Gavin M. Jones, Eric E. Knapp, Leda Kobziar, H. Millard, et al. Pyrosilviculture needed for landscape resilience of dry western united states forests. *Journal of Forestry*, 119(5):520–544, 2021.
- [2] Miguel G. Cruz, Martin E. Alexander, and Ronald H. Wakimoto. Development and testing of models for predicting crown fire rate of spread in conifer forest stands. *Canadian Journal of Forest Research*, 35(7):1626–1639, 2005.
- [3] Nicholas C. Coops, Piotr Tompalski, Tristan R.H. Goodbody, Martin Queinnec, and M. Queinnec. Modelling lidar-derived estimates of forest attributes over space and time: A review of approaches and future trends. *Remote Sensing of Environment*, 260:112477, 2021.
- [4] Kerri T. Vierling, Lee A. Vierling, William A. Gould, Sebastián Martinuzzi, and Rick M. Clawges. Lidar: shedding new light on habitat characterization and modeling. *Frontiers in Ecology and the Environment*, 6(2):90–98, 2008.
- [5] Camille S. Stevens-Rumann, Kerry B. Kemp, Philip E. Higuera, Brian J. Harvey, Monica T. Rother, Daniel C. Donato, Penelope Morgan, and Thomas T. Veblen. Evidence for declining forest resilience to wildfires under climate change. *Ecology Letters*, 21(2):243–252, 2018.
- [6] Michael A. Wulder, Christopher W. Bater, Nicholas C. Coops, Thomas Hilker, and Joanne C. White. The role of lidar in sustainable forest management. *The Forestry Chronicle*, 84(6):807–826, 2008.
- [7] Douglas K. Bolton, Nicholas C. Coops, Michael A. Wulder, Joanne C. White, Txomin Hermosilla, and Adam Collingwood. Optimizing landsat time series length for regional mapping of lidar-derived forest structure. *Remote Sensing of Environment*, 239:111645, 2020.
- [8] Susan Hummel, Andrew T. Hudak, Esker H. Uebler, Michael J. Falkowski, and Kevin A. Megown. A comparison of accuracy and cost of lidar versus stand exam data for landscape management on the malheur national forest. *Journal of Forestry*, 109(5):267–273, 2011.
- [9] Matthias Drusch, Umberto Del Bello, Sébastien Carlier, Olivier Colin, Veronica Fernandez, Ferran Gascon, Bianca Hoersch, Claudia Isola, Paolo Laberinti, Philippe Martimort, et al. Sentinel-2: Esa’s optical high-resolution mission for gmes operational services. *Remote Sensing of Environment*, 120:25–36, 2012.
- [10] J. Tolan, H.-I. Yang, B. Nosarzewski, et al. Very high resolution canopy height maps from rgb imagery using self-supervised vision transformer and convolutional decoder trained on aerial lidar. *Remote Sensing of Environment*, 300:113888, 2024.
- [11] LANDFIRE. Landfire fuels - forest canopy height. Technical report, U.S. Geological Survey, 2022.
- [12] N. Lang, W. Jetz, K. Schindler, and J.D. Wegner. A high-resolution canopy height model of the earth. *Nature Ecology & Evolution*, 7:1778–1789, 2023.
- [13] Tony Chang, Kiarie Ndegwa, Andreas Gros, Vincent A. Landau, Luke J. Zachmann, B. State, M.A. Gritts, C.W. Miller, Nathan E. Rutenbeck, Scott Conway, and Guy Bayes. Vibrantvs: A high-resolution multi-task transformer for forest canopy height estimation. *Remote Sensing*, 17(6):1017, 2025. doi: 10.3390/rs17061017.

[14] U.S. Environmental Protection Agency. Level iii ecoregions of the continental united states. Technical report, U.S. Environmental Protection Agency, 2013.

[15] Fabien H. Wagner, Ricardo Dalagnol, Yuliya Tarabalka, Karl Segl, et al. Sub-meter tree height mapping of california using aerial images and lidar-informed u-net model. *Remote Sensing of Environment*, 305:114099, 2024.

[16] Katherine M. Thibault et al. The us national ecological observatory network and the global biodiversity framework. *Journal of Ecology and Environment*, 47, 2023.

[17] Wojciech Sirko, Emmanuel Asiedu Brempong, Juliana TC Marcos, Abigail Annkah, Abel Korme, Mohammed Alewi Hassen, Krishna Sapkota, Tomer Shekel, Abdoulaye Diack, Sella Nevo, Jason Hickey, and John Quinn. High-resolution building and road detection from sentinel-2. *arXiv preprint arXiv:2310.11622*, 2023.

[18] Jun Ma, Michael Schmitt, and Xiao Xiang Zhu. Opensr: Scalable and trustworthy super-resolution for satellite imagery. *IEEE Transactions on Geoscience and Remote Sensing*, 2023.

[19] Michael Schmitt, Lloyd Hughes, Chunping Qiu, and Xiao Xiang Zhu. Sen12ms-cr: A remote sensing dataset for multimodal multi-coverage image classification and regression. *IEEE Transactions on Geoscience and Remote Sensing*, 2023.

[20] Charis Lanaras, José Bioucas-Dias, Silvano Galliani, Emmanuel Baltsavias, and Konrad Schindler. Super-resolution of sentinel-2 images: Learning a globally applicable deep neural network. *ISPRS Journal of Photogrammetry and Remote Sensing*, 146:305–319, 2018.

[21] Patrick A. G. Watson et al. Generative deep learning for climate downscaling. *Journal of Advances in Modeling Earth Systems*, 13(10), 2021.

[22] Ilan Price et al. Generative models for downscaling climate data. *Proceedings of the National Academy of Sciences*, 2023.

[23] Xingchao Liu, Chengyue Gong, and Qiang Liu. Flow straight and fast: Learning to generate and transfer data with rectified flow. In *International Conference on Learning Representations (ICLR)*, 2023.

[24] Yaron Lipman, Ricky T. Q. Chen, Heli Ben-Hamu, Maximilian Nickel, and Matt Le. Flow matching for generative modeling. In *International Conference on Learning Representations (ICLR)*, 2023.

[25] Patrick Esser, Sumith Kulal, Andreas Blattmann, Rahim Entezari, Jonas Müller, Harry Saini, Yam Levi, Dominik Axelrod, Robin Rombach, et al. Scaling rectified flow transformers for high-resolution image synthesis. In *International Conference on Machine Learning (ICML)*, 2024.

[26] Element 84. Earth search stac api: Sentinel-2 collection 1 level-2a (sentinel-2-c1-l2a). <https://github.com/Element84/earth-search>, 2023. README documentation describing the Earth Search STAC API and the sentinel-2-c1-l2a collection. Accessed 2026-01-08.

[27] U.S. Geological Survey. 3d elevation program (3dep). Technical report, U.S. Geological Survey, 2024.

- [28] Martin Van Leeuwen and Maarten Nieuwenhuis. Retrieval of forest structural parameters using lidar remote sensing. *European Journal of Forest Research*, 129(4):749–770, 2010.
- [29] Yaron Lipman, Marton Havasi, Peter Holderrieth, Neta Shaul, Matt Le, Brian Karrer, Ricky T. Q. Chen, David Lopez-Paz, Heli Ben-Hamu, and Itai Gat. Flow matching guide and code, 2024. URL <https://arxiv.org/abs/2412.06264>.
- [30] Ricky T. Q. Chen, Yulia Rubanova, Jesse Bettencourt, and David K. Duvenaud. Neural ordinary differential equations. In *Advances in Neural Information Processing Systems*, 2018. URL <https://arxiv.org/abs/1806.07366>.